Wheel–rail dynamics with closely conformal contact Part 1: dynamic modelling and stability analysis

A Bhaskar, **K L Johnson**, **G D Wood** and **J Woodhouse**
Engineering Department, Cambridge University

Abstract: Observations on the Vancouver mass transit system suggest that noise, vibration and corrugation of the rail appear to be associated with close conformity between the transverse profiles of the wheel and rail. To investigate this, a dynamic model of the wheel and rail under conditions of close conformity has been developed. Previous work has suggested that motion of the wheel could be neglected, so the model comprises two subsystems: (a) the rail and its supports, and (b) the contact between wheel and rail. A dynamic model of a continuously supported rail is presented, which is consistent with similar models in the literature. Conformal contact has been represented in two ways: (a) as a single highly eccentric elliptical contact, and (b) as a two-point contact. Novel 'rolling contact mechanics' have been incorporated in both these models. The complete system is closed: oscillations of the rail give rise to fluctuating contact forces, which in turn excite the rail. A linear stability analysis of the system shows it to be stable under all conditions examined, thus precluding the possibility of self-excited oscillations occurring on a perfectly smooth rail. The model can then be used to investigate the forced response to existing roughness on the railhead, which is the subject of a companion paper (**1**).

Keywords: wheel–rail, contact, corrugation, conformity

NOTATION

The convention is used throughout that any quantity X may be expressed as $X_0 + X'$, denoting respectively the steady component and the harmonically fluctuating component.

a, b, c	semi-axes of contact ellipse, $c = \sqrt{(ab)}$
$\mathbf{A}$	see equation (14)
$\mathbf{B}$	see equation (12)
$\boldsymbol{c}$	see equation (25)
C_{ij}	creep coefficients
$\mathbf{D}$	see equation (28)
$\boldsymbol{e}$	see equation (28)
$\mathbf{F}$	see equation (30)
$\boldsymbol{g}$	see equation (30)
G	shear modulus
$\mathbf{H}_R$	rail receptance matrix
$\mathbf{H}_1$, $\mathbf{H}_2$	general transfer function matrices
$\boldsymbol{j}$	see equation (28)
k	wave number
k_H	'Hertz' spring stiffness
K	conformity factor $= \rho/(\rho - r)$
$\mathbf{K}$	rail stiffness matrix
M	rail moment
$\mathbf{M}$	rail mass matrix
M_z	spin moment
N	normal rail force
P	normal contact force
Q_x, Q_y	components of tangential contact force Q
r	rail profile radius
r_1, r_2	see Appendix 2
R_1	wheel radius
R_2	$= Kr$; $R_e = \sqrt{(R_1 R_2)}$
s	spin pole position
$\boldsymbol{s}$	see equation (20)
$\mathbf{S}$	see equation (20)
T	tangential rail force
$\boldsymbol{u}$	vector of generalized coordinates
U	rail potential energy
v_x, v_y, v_z	velocity components of rail relative to wheel at contact point
V	train speed
w_2, w_3	rail displacement components
W	frictional power dissipation
x, y, z	contact coordinates
α	contact angle (see Figs 5 and 9)
δ_x, δ_y, δ_z	components of contact displacement
Δ	input displacement
η	see equation (15)
θ	angular displacement of contact point

The MS was received on 18 December 1996 and was accepted for publication on 14 April 1997.

λ	conicity angle
μ	coefficient of friction
v	Poisson's ratio
ξ_x, ξ_y, ξ_z	components of creepage
ρ	wheel profile radius
ϕ	rail rotation
ψ	input rotation
ω	angular frequency
ω_z	spin angular velocity

1 INTRODUCTION

1.1 The Intercity scene

The propensity of railway rails to develop corrugations or ripples on the running surface through the action of the wheels has been observed throughout railway history. The nature and wavelength of the ripples are varied. Grassie and Kalousek (**2**) have recently presented a detailed review of their different characteristics, causes and treatments. The short-pitch (30–60 mm) corrugations found on the passenger railways of Europe have been particularly resistant to explanation and modelling. The most satisfactory theory at the present time is that presented by Hempelmann and Knothe (**3**), which is based on a hypothesis advanced by Frederick (**4**) and Valdivia (**5**). In outline, the hypothesis is that the dynamic characteristics of the wheel–rail system, in response to excitation by random roughness of the running surface of the rail, acts as a filter such that the dynamic contact force is amplified in one or more narrow bands of frequency. A 'damage mechanism', in this case wear, then gives rise to a slow progressive modification to the initial random profile in those distinct frequency bands. If the phase of the periodic wear is appropriate, the random profile will develop into a regular wave which deepens progressively with time.

For Intercity track, in which the rail is supported by concrete sleepers in ballast through a soft rail pad, two such frequencies have been identified: one at an anti-resonance associated with the so-called 'pinned-pinned resonance', when the rail bends into a half-wavelength between adjacent sleeper supports (occurring in the range 800–1100 Hz depending on sleeper spacing); the other in which the sleeper acts as a dynamic vibration absorber attached to the rail through the elastic rail pad (occurring in the range 300–500 Hz). With fixed critical frequency bands it would be expected that the corrugation pitch would vary in direct proportion to the vehicle speed, whereas the wavelengths observed in practice vary little with train speed. This paradox is explained in Hempelmann's theory by his finding that at wavelengths less than 1.5 times the contact patch length (i.e. about 20 mm) the phase of the incremental wear is such as to attenuate any incipient corrugation. Thus, it is argued, with high-speed passenger trains the 'pinned-pinned' frequency is dominant, producing corrugations of about the observed wavelength (40–50 mm). With lower speed (freight) traffic this frequency band is inactive since it would produce corrugations of wavelength less than 20 mm. The 300–400 Hz band is then active, again producing corrugations of the observed wavelength. In this way mixed traffic can reinforce waves of roughly the same pitch.

1.2 The urban mass transit scene

More recently, new mass transit systems in the large cities of the world have frequently developed short-pitch corrugations soon after opening, which has led to a heightened awareness of the problem. In Vancouver, six months after the opening in 1986 of the 'Skytrain', 85 per cent of the track was corrugated and the noise level was very high. This led to an in-depth investigation of the problem reported by Kalousek and Johnson (**6**), which gave rise to the present project. The most important conclusions of that investigation for the purpose of the present study may be summarized as follows:

1. Vehicles are driven and braked by linear induction motors, so that no driving or braking forces are exerted at the wheel treads.
2. Examination by scanning electron microscope of replicas of the running surface revealed periodic scratch marks, of typical length 100 μm, suggestive of roll–slip oscillations at the wheel contacts.
3. The application of a solid lubricant to the wheel treads reduced the noise level.
4. Steered trucks (bogies) and unusually accurate control of the track gauge promoted rapid wear of the wheel treads to a profile which was closely conformal with the transverse profile of the rail.
5. Grinding sections of the system to different rail profiles, such that contact was made at different locations on the wheel treads, prevented wear to close conformity and was found to slow down drastically the formation of corrugations.
6. Remote control of the trains ensures that they travel over any prescribed location at the same known speed. This enabled the variation of corrugation wavelength with speed to be obtained more precisely than hitherto. It is shown in Fig. 1. The wavelength increased from about 30 mm at 20 km/h to about 45 mm at 85 km/h. This corresponds to a variation in vibration frequency from 200 to 550 Hz. The results are in good agreement with such results as are available for British Rail track, also shown in Fig. 1.
7. The spacing of the track supports changed by a factor of two between straight and curved track, but the pattern of corrugation wavelength was unaffected.

These observations suggest that wear of the wheel treads into close conformity with the rail somehow promoted oscillatory behaviour and periodic slip. The variation of wavelength with vehicle speed in Fig. 1 is suggestive of a roll–slip oscillation in which the roll phase corresponds to

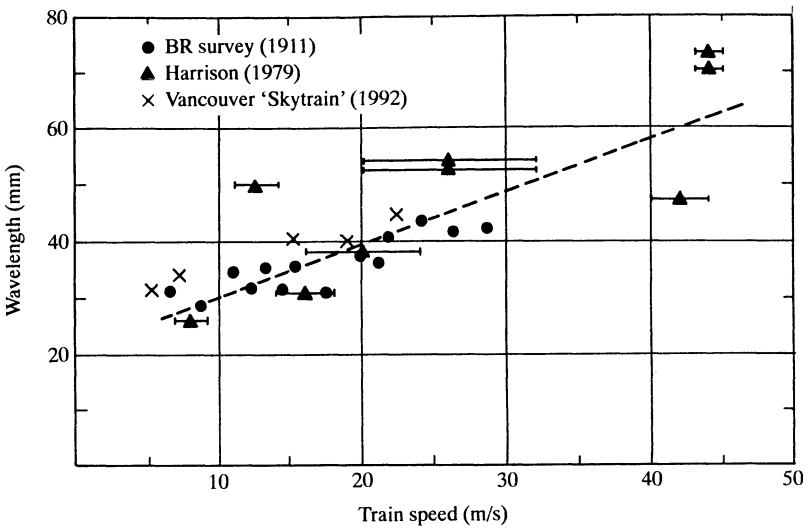

Fig. 1 Variation of mean corrugation wavelength with train speed (**2**, **6**)

a fixed *distance* along the rail (about 30 mm) and the slip phase to a fixed *time* (about 0.55 ms). Accordingly, the present investigation was started with the object of modelling the dynamic behaviour of conformal wheel–rail contacts.

1.3 Outline of the present investigation

As a necessary prelude to direct non-linear modelling of 'roll–slip' oscillations, a linear dynamic model of wheel–rail contact has been developed. This enables the stability of the system to be assessed, so as to discover whether close conformity could lead to self-excited oscillations, perhaps analogous to those occurring during bogie hunting. It also permits an economical parametric survey of the sensitivity of a conformal contact to excitation by rail roughness. Finally, it allows an assessment to be made of whether predictions of the (linearized) Hempelmann–Knothe theory are significantly altered by close conformity between wheel and rail.

The system comprises two subsystems: (a) the rail and its supports; and (b) the contact of the wheel with the rail. Relative motion between the wheel and the rail gives rise to dynamic normal and tangential (creep) forces at the point (or points) of contact. Contact forces acting on the rail excite bending and torsional oscillations of the rail which, in turn, influence the contact motion, resulting in a closed-loop system. External forcing is provided by surface irregularities on the wheel or rail. Energy is supplied by forward motion of the wheel through the action of steady longitudinal and/or lateral creepage, so that the possibility exists for dynamic instability. The two subsystems, 'rail dynamics' and 'contact mechanics', will be modelled separately and subsequently brought together under conditions of close conformity between the transverse profiles of the rail and the wheel tread.

On the basis of earlier work (**7**) it was concluded that the impedance of the wheel rim compared with that of the rail was sufficiently high to neglect motion of the wheel except in a few very narrow frequency bands. In the work reported here the wheel has been taken to be rigid.

2 THE RAIL MODEL

For the purpose of studying the effect of close conformity it was essential to have a rail model capable of accurately predicting the lateral and rotational motion of the rail in the frequency range 0–2000 Hz. There are in the literature two styles of model which, in principle, satisfy this condition, one by Thompson (**8**) based on finite element computations, and the other by Ripke and Knothe (**9**) in which the rail section is built up by separately representing the head by a beam in bending and torsion, and the web and foot by plates. The approach followed here is a development of the latter, and is illustrated in Fig. 2.

A variational model has been developed for harmonic waves on an infinite rail, which is assumed to be continuously supported by uniformly distributed rail pads, sleeper mass and ballast. Although it would have been possible to incorporate discrete supports into the model, the observation on the Vancouver mass transit that the corrugation wavelength was independent of a change in spacing of the supports encouraged the authors to take advantage of the simplicity of a continuous support model. Motion of the railhead in the cross-sectional plane may be characterized by two independent in-plane displacements and an in-plane rotation. The deformation of the plates AB, BC and BD perpendicular to their planes (see Fig. 2) is approximated in each case by a cubic function, while in the plane they are allowed uniform displacement only. Thus each plate contributes five additional degrees of freedom. This number is

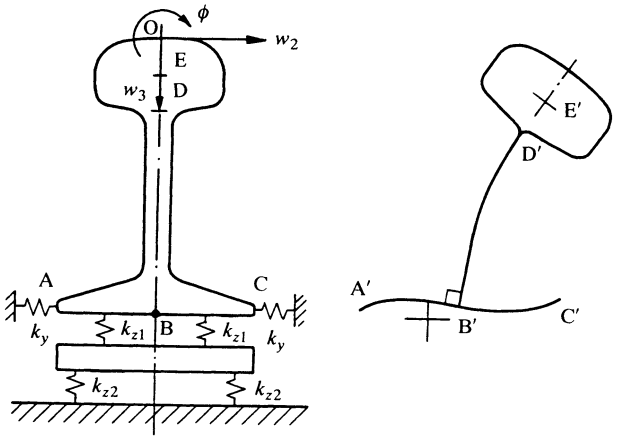

Fig. 2 Cross-sectional details of the rail model, showing the continuous support, and the skeleton of the rail section showing (at exaggerated scale) the allowed cross-sectional deformation

reduced when continuity conditions are allowed for: both components of displacement and also the rotation must be continuous at the points B′ and D′, so that nine conditions must be imposed. Thus the remaining number of independent degrees of freedom contributed by this motion of the three plates is just six. Finally, axial motion is allowed for: uniform axial motion is associated with compressional waves in the rail, and differential motion in the axial direction is associated with bending waves in the rail.

The railpads and ballast are represented by linear springs with hysteretic damping. Separate sets of springs act vertically and laterally. The spacing of the points of attachment to the base plates is set equal to the width of the rail foot divided by $\sqrt{3}$ so that the correct moment impedance is obtained, once the vertical and lateral spring stiffnesses have been adjusted to conform with previously measured values (**7**). When modelling the Vancouver track, the pads are attached to a rigid slab. For European Intercity track the pads are attached to sleepers supported in ballast, with the sleeper mass distributed uniformly along the track. In this latter case, an additional degree of freedom to describe the vertical displacement of the sleeper mass is needed.

Expressions may then be derived for the kinetic and potential energies per unit length of rail under the assumed deformation when a harmonic travelling wave $e^{i(kx-\omega t)}$ is imposed. Although the details are somewhat complicated, these formulae are made up entirely from standard expressions. For the railhead, the strain energy expressions involve deformations as a beam in bending, a bar in axial compression and a shaft in torsion. The strain energy expressions used for the web and base plates allow for out-of-plane bending and twisting deformations, and axial compression. Finally, the potential energy in the foundation springs must be added. The kinetic energy expression is obtained more straightforwardly, by considering the motion of each point of the rail section, and of the sleeper mass, during the assumed deformation.

Assuming that all displacements are small, both kinetic and potential energy expressions can be approximated by quadratic forms in the assumed generalized coordinates, as usual: writing $U(k)$ for the potential energy, $T(\omega)$ for the kinetic energy and $\boldsymbol{u}$ for the vector of generalized coordinates

$$U(k) = \tfrac{1}{2}\boldsymbol{u}^{\mathrm{t}}\mathbf{K}(k)\boldsymbol{u}$$
$$T(\omega) = -\tfrac{1}{2}\omega^2\boldsymbol{u}^{\mathrm{t}}\mathbf{M}\boldsymbol{u} \tag{1}$$

where $\mathbf{K}(k)$ and $\mathbf{M}$ are the stiffness and mass matrices, k is the wave number of the assumed travelling wave, and ω is the angular frequency. Because of the orders of derivatives which are included in the various expressions for strain energy, the matrix $\mathbf{K}(k)$ takes the form of a quadratic expression in k^2.

Applying Hamilton's principle, or equivalently by making the Rayleigh quotient stationary, the dispersion relation is obtained from the condition for non-trivial solutions

$$D(k, \omega) \equiv \det[\mathbf{K}(k) - \omega^2\mathbf{M}] = 0 \tag{2}$$

Roots of this equation, most conveniently expressed as a family of solutions $k(\omega)$, describe the behaviour of possible propagating and evanescent waves on the rail. Dispersion curves for the propagating waves for a BS113A rail are shown in Fig. 3. The various branches of the dispersion relation are associated with different kinds of motion of the rail section and its supporting sleeper mass. Five wave types can propagate from low cut-on frequencies. Three of these, associated with lateral bending, vertical bending and torsion, are particularly important to this study. The other

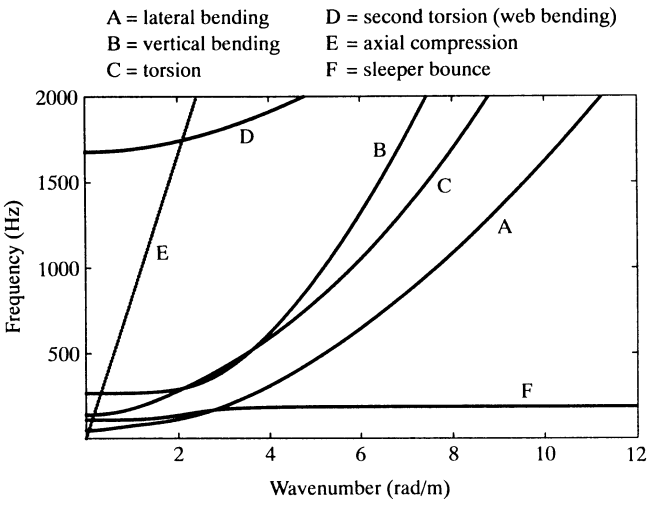

Fig. 3 Dispersion curves for wave propagation on BR track (BS113A) using the continuous support model developed here

two are (a) a steeply rising line representing axial compressional waves in the rail, and (b) a line which tends towards the horizontal at high wave numbers, associated with bouncing of the sleeper mass beneath an immobile rail. The details of the picture at low frequencies and wave numbers are quite complicated, as the various types of motion couple together there. A sixth wave type (involving web bending in the rail section) appears above a cut-on frequency which is about 1700 Hz in the results of this study. At frequencies below this cut-on the associated rail motion is evanescent.

It is necessary to calculate the response of the rail in the cross-sectional plane to harmonic loading applied at a reference point on the railhead. It is convenient to choose the mid-point O, since the rail sections and supports are symmetrical about the centre line of the section. The rail response can then be written in terms of a Fourier integral, from which the matrix of receptances can be extracted

$$\mathbf{H}(x, \mathrm{i}\omega) = \frac{1}{2\pi}\int_{-\infty}^{\infty} [\mathbf{K}(k) - \omega^2\mathbf{M}]^{-1}\, \mathrm{e}^{-\mathrm{i}kx}\, \mathrm{d}k \tag{3}$$

The integral can be evaluated by contour integration, taking advantage of the known analytic dependence on wave number k to evaluate the residues at the poles of the integrand. The symmetry about O means that the normal receptance H_{33} is independent of lateral and rotational motion, governed by receptances H_{22}, H_{44} and H_{24}. Thus the railhead motions w_2, w_3 and ϕ are related to the harmonically fluctuating com- ponents of applied lateral force T', normal force N' and moment M' by the matrix relation

$$\begin{bmatrix} w_2 \\ w_3 \\ \phi \end{bmatrix} = \begin{bmatrix} H_{22} & 0 & H_{24} \\ 0 & H_{33} & 0 \\ H_{24} & 0 & H_{44} \end{bmatrix} \begin{bmatrix} T' \\ N' \\ M' \end{bmatrix} \equiv \mathbf{H}_{\mathrm{R}} \begin{bmatrix} T' \\ N' \\ M' \end{bmatrix} \tag{4}$$

(The slightly curious index convention is used because the axial motion w_1 plays no part here.) Driving-point receptances H_{ij} to harmonic excitation at the mid-point O of the railhead are shown in amplitude and phase in Fig. 4a to d, for Intercity track comprising BS113A rail together with sleepers and ballast as shown in Fig. 2. Good agreement is found with the predictions of Ripke's model, shown superimposed on the figures. The only regions of significant disagreement are narrow bands of enhanced or reduced response associated with discrete sleeper supports, allowed for in Ripke's model and absent in that of the authors.

3 CONTACT MECHANICS

3.1 Low-spin model

3.1.1 Steady creepage

The contact of a wheel tread (profile radius ρ) with a rail (profile radius r) is shown in Fig. 5. The contact point subtends an angle α with the centre line of the rail cross-section, which in turn lies at an angle λ to the vertical. Based on the analysis by Johnson ((**10**), pp. 260–262) the following relationships are proposed for interactive steady state creepage (involving creepage components in both x and y directions):

$$C_{11}\xi_x = \frac{3\mu P}{Gc^2}\frac{Q_x}{Q}\left[1 - \left(1 - \frac{Q}{\mu P}\right)^{1/3}\right] \tag{5a}$$

and

$$C_{22}\xi_y + C_{23}\frac{c\sin(\lambda+\alpha)}{R_1} = \frac{3\mu P}{Gc^2}\frac{Q_y}{Q}\left[1 - \left(1 - \frac{Q}{\mu P}\right)^{1/3}\right] \tag{5b}$$

where ξ_x and ξ_y are longitudinal and lateral creepages; Q_x and Q_y are corresponding tangential creep forces; C_{11}, C_{22} and C_{23} are Kalker's creep coefficients (**11**); R_1 is the rolling radius of the wheel; P is the normal load; μ is the coefficient of friction; $c = (ab)^{1/2}$, where a and b are the semi-axes of the contact area; and

$$Q = (Q_x^2 + Q_y^2)^{1/2} \tag{6}$$

To remove a minor inconsistency at saturated creepage, it is convenient to replace C_{11} and C_{22} (which are of similar magnitude) by their average $C_{00} = (C_{11} + C_{22})/2$.

The relative radius of curvature between the wheel and the rail is given by

$$R_2 = \frac{\rho r}{\rho - r} = Kr \tag{7}$$

where $K = \rho/(\rho - r)$ characterizes the degree of conformity. Following Johnson ((**10**), pp. 96–97), the Hertz theory for mildly elliptical contacts gives

$$\frac{b}{a} \approx \left(\frac{R_2}{R_1}\right)^{2/3} = \left(\frac{Kr}{R_1}\right)^{2/3} \tag{8}$$

and

$$c = (ab)^{1/2} \approx \left[3(1-\nu)\frac{R_{\mathrm{e}}P}{4G}\right]^{1/3} \tag{9}$$

where G is the shear modulus, ν is Poisson's ratio, and

$$R_{\mathrm{e}} = (R_1 R_2)^{1/2}$$

The compression δ_z of the contact is expressed by

$$\delta_z = \left[\frac{9(1-\nu)^2 P^2}{16G^2 R_{\mathrm{e}}}\right]^{1/3} \tag{10}$$

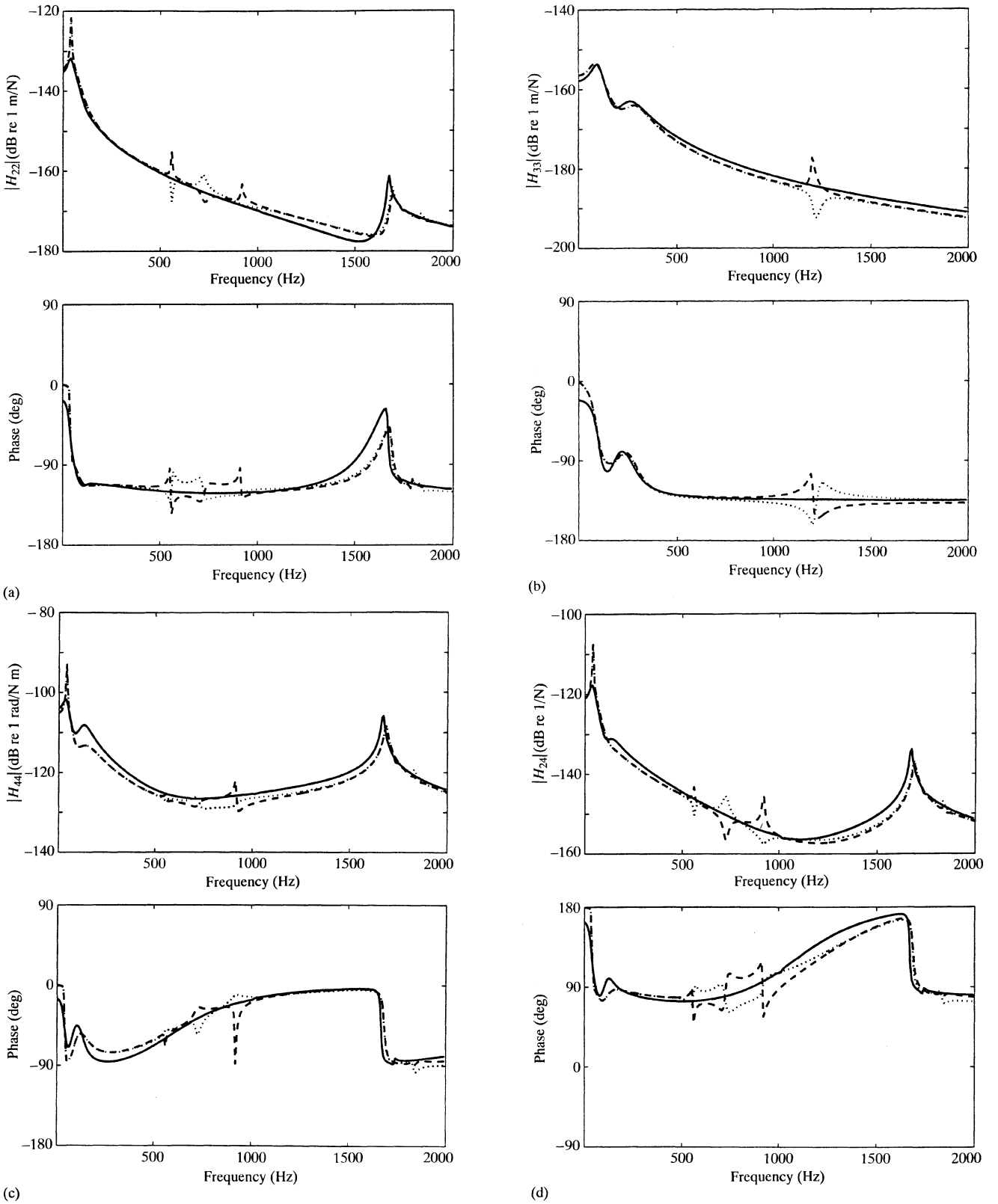

Fig. 4 Receptance curves (solid lines) for rail motion in the transverse plane, for point excitation at the mid-point of the railhead: (a) lateral direct receptance $H_{22} = w_2/T$; (b) vertical direct receptance $H_{33} = w_3/N$; (c) rotational direct receptance $H_{44} = \phi/M$; (d) cross receptance $H_{24} = w_2/M = \phi/T$. Results from Ripke's calculations (**9**), for Intercity track having similar parameters, are shown for comparison, mid-way between sleepers (dashed lines) and at a sleeper (dotted lines)

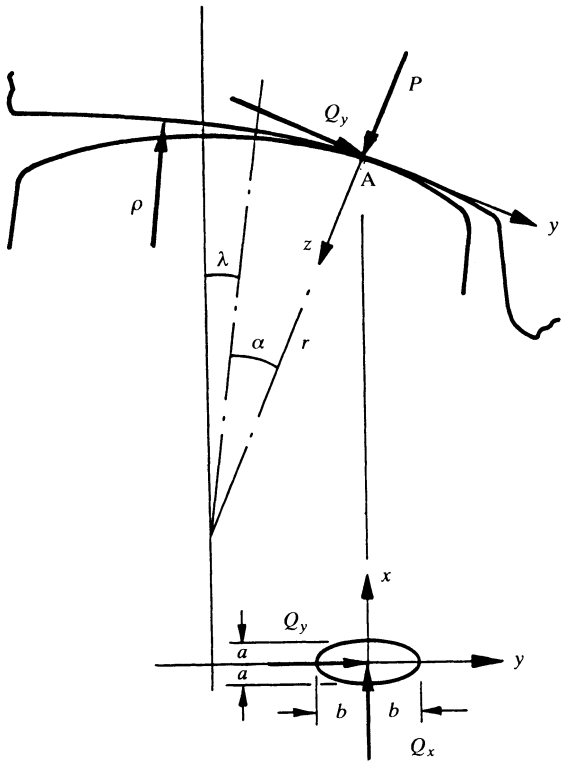

Fig. 5 Wheel–rail contact geometry for a single contact point: λ is the nominal conicity of the wheel

which gives the linearized stiffness of the 'Hertz spring' at $P = P_0$:

$$k_{\mathrm{H}} = \left(\frac{\mathrm{d}P}{\mathrm{d}\delta_z}\right)_0 = \left[\frac{6G^2 P_0 R_{\mathrm{e}}}{(1-\nu)^2}\right]^{1/3} \tag{11}$$

The effect on steady state creepages of small changes in force, Q'_x, Q'_y, P', from a reference state Q_{x0}, Q_{y0}, P_0, is given by differentiation of equations (5a and b):

$$\begin{bmatrix} \xi'_x \\ \xi'_y \\ \xi'_z \end{bmatrix} = \begin{bmatrix} \dfrac{\partial \xi_x}{\partial Q_x} & \dfrac{\partial \xi_x}{\partial Q_y} & \dfrac{\partial \xi_x}{\partial P} \\ \dfrac{\partial \xi_y}{\partial Q_x} & \dfrac{\partial \xi_y}{\partial Q_y} & \dfrac{\partial \xi_y}{\partial P} \\ 0 & 0 & 0 \end{bmatrix} \begin{bmatrix} Q'_x \\ Q'_y \\ P' \end{bmatrix} \tag{12}$$

where $\xi_x = \xi_{x0} + \xi'_x$ and $\xi_y = \xi_{y0} + \xi'_y$. The vertical 'creepage' ξ_z is also included for compatibility with later matrix equations, but it is uninfluenced by the lateral creepage and is determined only by the Hertz spring stiffness, to be allowed for in the next subsection. The matrix in equation (12) is denoted by **B**; expressions for the derivatives are quoted in Appendix 1.

3.1.2 Transient creepage

With rapid changes in force, the creepage experiences a transient delay in reaching the steady state. This effect has been analysed in detail by Gross-Thebing (**12**). A simplified treatment of transient creepage in closed form is used here, based on the notion of 'tangential contact springs' acting in series with the 'creepage dashpots' which represent the velocity-dependent behaviour of equation (12). Details of the model are presented in Appendix 1.

It is required to calculate the response to small harmonic variations in force Q'_x, Q'_y and P' from a steady reference state in which the steady creepages are ξ_{x0} and ξ_{y0} and the forces are Q_{x0}, Q_{y0} and P_0. It is shown in Appendix 1 that in response to harmonic variations in force of angular frequency ω, there are harmonic variations in velocity v'_x, v'_y, v'_z of the rail relative to the wheel at the point of contact, given by

$$\frac{1}{V}\begin{bmatrix} v'_x \\ v'_y \\ v'_z \end{bmatrix} = \left[\frac{\mathrm{i}\omega}{V}\mathbf{A} + \mathbf{B}\right]\begin{bmatrix} Q'_x \\ Q'_y \\ P' \end{bmatrix} \tag{13}$$

where V is the vehicle speed. The matrix **A** allows for the elastic transient effects, as well as the vertical Hertz spring. It can be written

$$\mathbf{A} = \begin{bmatrix} a_{11} & 0 & 0 \\ 0 & a_{22} & 0 \\ 0 & 0 & a_{33} \end{bmatrix} \tag{14}$$

where the coefficients a_{11} and a_{22} are given in Appendix 1; a_{33} is the compliance of the Hertz spring $1/k_{\mathrm{H}}$, given by equation (11). The matrix **B** is that of the derivatives of steady creepage, expressed by equation (12).

3.2 High-spin model

Under conditions of close conformity the ellipse of contact becomes long and thin ($b \gg a$), so that the theory underlying equation (5a and b) becomes a poor approximation and a 'strip theory' becomes more appropriate [see reference (**10**), p. 268]. If the spin creep is high, as a result of the large values of b, an approximation to the contact mechanics can be obtained in closed form by neglecting tangential compliance compared with the slip [see reference (**10**), p. 259]. In this simplification there is a point, labelled C in Fig. 6, where, in the absence of lateral slip, there would be no relative velocity between the surfaces. This point C is known as the 'spin pole'. Let it be a distance sb from the centre of the contact O. The longitudinal creepage ξ''_x experienced by a strip at location y is then given by

$$\xi''_x = \xi_x - \frac{y\omega_z}{V} = \xi_x - \left(\frac{\omega_z b}{V}\right)\eta \tag{15}$$

where $\eta = y/b$ and ω_z is the angular velocity of spin. In the wheel–rail contact of Fig. 5

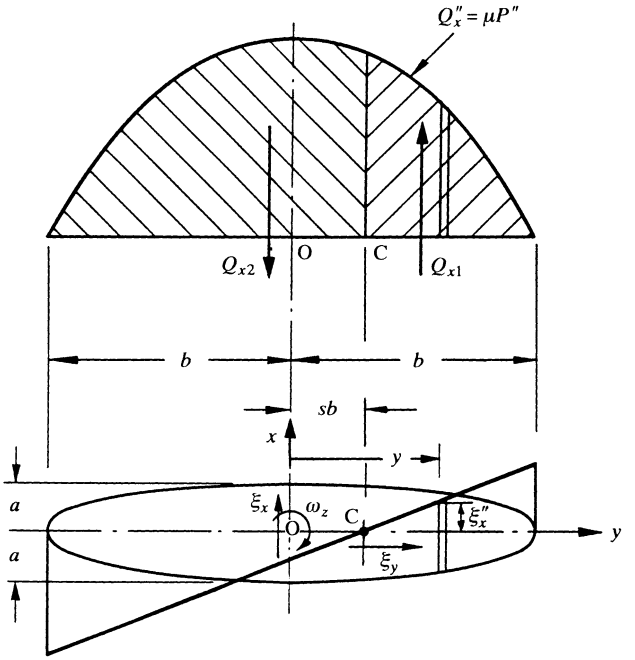

Fig. 6 Strip theory analysis used to obtain the high-spin contact model for the case of close conformity ($b \gg a$)

$$\frac{\omega_z b}{V} = \left(\frac{b}{R_1}\right)\sin(\lambda+\alpha)$$

at the spin pole $\xi''_x = 0$, so that $s = (\xi_x V/\omega_z b)$

Now the longitudinal traction force per unit width acting on the strip is

$$Q'' = \mu P'' = \left(\frac{3\mu P}{4b}\right)(1-\eta^2) \tag{16}$$

The traction force Q_{x1} acting to the right of the spin pole in Fig. 6 is thus given by

$$Q_{x1} = \int_{sb}^{b} Q''\,\mathrm{d}y = \tfrac{1}{4}\mu P(2-3s+s^3) \tag{17a}$$

and that to the left of C by

$$Q_{x2} = -\int_{-b}^{sb} Q''\,\mathrm{d}y = -\tfrac{1}{4}\mu P(2+3s-s^3) \tag{17b}$$

whereupon

$$Q_x = Q_{x1} + Q_{x2} = -\tfrac{1}{2}\mu P(3s-s^3) \tag{17c}$$

The spin moment M_z is given by the sum of the moments of Q_{x1} and Q_{x2} about O, i.e.

$$M_z = M_{z1} + M_{z2}$$

where the two components turn out to be equal

$$\begin{aligned} M_{z1} &= -\frac{3\mu Pb}{4}\int_s^1 (1-\eta^2)\eta\,\mathrm{d}\eta \\ &= M_{z2} = \frac{3\mu Pb}{4}\int_{-1}^{s}(1-\eta^2)\eta\,\mathrm{d}\eta \\ &= -\frac{3\mu Pb}{16}(1-s^2)^2 \end{aligned} \tag{18}$$

It is now necessary to incorporate lateral creepage ξ_y, and its interaction with longitudinal and spin creepage. This is done in Appendix 2, where the relationships between the creep forces and moment and the creepages are shown to be

$$Q_x = \frac{\mu P}{4}\left[\frac{(1-s)}{r_1}(2-3s+s^3) - \frac{(1+s)}{r_2}(2+3s-s^3)\right] \tag{19a}$$

$$Q_y = -\frac{\mu P}{4}\left[\frac{t}{r_1}(2-3s+s^3) + \frac{t}{r_2}(2+3s-s^3)\right] \tag{19b}$$

and

$$M_z = -\frac{3\mu Pb}{16}\left[\frac{(1-s)}{r_1}(2-3s+s^3) + \frac{(1+s)}{r_2}(2+3s-s^3)\right] \tag{19c}$$

in terms of dimensionless ratios t, r_1 and r_2 defined in Appendix 2.

In this treatment, where the elastic strains are neglected compared with the slip, the transient creep effect contained in matrix **A** in Appendix 1 does not arise. The linear contact mechanics model for harmonically oscillating creepage then becomes

$$\begin{bmatrix} Q'_x \\ Q'_y \\ P' \end{bmatrix} = \begin{bmatrix} S_{11} & S_{12} & S_{13} \\ S_{21} & S_{22} & S_{23} \\ 0 & 0 & S_{33} \end{bmatrix} \begin{bmatrix} \xi'_x \\ \xi'_y \\ \xi'_z \end{bmatrix} + \xi_s \cot(\lambda+\alpha) \begin{bmatrix} b_1 \\ b_2 \\ 0 \end{bmatrix} \theta \equiv \mathbf{S} \begin{bmatrix} \xi'_x \\ \xi'_y \\ \xi'_z \end{bmatrix} + \boldsymbol{s}\theta \tag{20}$$

where S_{ij} are the derivatives of equations (19a) and (19b) with respect to ξ_x, ξ_y and ξ_z after P has been expressed in terms of ξ'_z via the Hertz spring relation

$$S_{33} = -\frac{Vk_{\mathrm{H}}}{i\omega} \tag{21}$$

where k_H is given by equation (11). The second term in equation (20) involves the quantities $b_1 = \partial Q_x/\partial \xi_s$, $b_2 = \partial Q_y/\partial \xi_s$ and $\theta(= \alpha')$, which is the angle subtended by the displacement of the contact point from its reference position.

The fluctuations in spin moment are found from

$$M'_z = [p_1\, p_2\, p_3] \begin{bmatrix} \xi'_x \\ \xi'_y \\ \xi'_z \end{bmatrix} \tag{22}$$

where p_i are the derivatives of equation (19) with respect to ξ_x, ξ_y and ξ_z. The fluctuating power dissipation W', including the spin loss, is given by

$$\frac{W'}{V} = -Q_{x0}\xi'_x + Q_{y0}\xi'_y + \frac{M_{z0}}{R_1}\cos(\lambda+\alpha)\theta + Q'_x\xi_{x0} + Q'_y\xi_{y0} + \frac{M'_z}{R_1}\sin(\lambda+\alpha) \tag{23}$$

The question arises: under what conditions is the high-spin model appropriate? The relevant parameter is $[b\sin(\lambda+\alpha)/\mu a]$; the model becomes a reasonable approximation when the value of this parameter exceeds 1.0. Clearly its value increases with conformity as the ratio b/a for the contact ellipse increases. The reference conditions examined below and in the companion paper (**1**) correspond to a value of approximately 1.5.

4 CONFORMAL CONTACT

4.1 Single moving point of contact

A significant feature of a closely conforming contact is that small lateral and rotational displacements of the rail relative to the wheel can cause a relatively large movement of the contact point across the railhead. The geometry is shown in Fig. 7. In the steady reference state the contact point is located at A_0. Oscillating rail displacements w_2, w_3 and ϕ are assumed to be excited by a ripple on the wheel or rail surface which imposes a normal displacement $\Delta\, e^{i\omega t}$ at A_0 and a rotation $\psi\, e^{i\omega t}$. The combination of the imposed ripple and the rail motion causes an oscillatory lateral motion $r\theta$ of the point of contact where, in the context of a linear theory, θ must be assumed small. From the geometry of Fig. 7, it follows that the shift of the point of contact from A_0 to A is given by

$$A_0A = r\theta = K[r\psi + (w_2 - r\phi)\cos\alpha + w_3\sin\alpha] \tag{24}$$

so that θ may be written in the form

$$\theta = K\left(\psi + \boldsymbol{c}^t \begin{bmatrix} w_2 \\ w_3 \\ \phi \end{bmatrix}\right) \qquad \text{with}$$

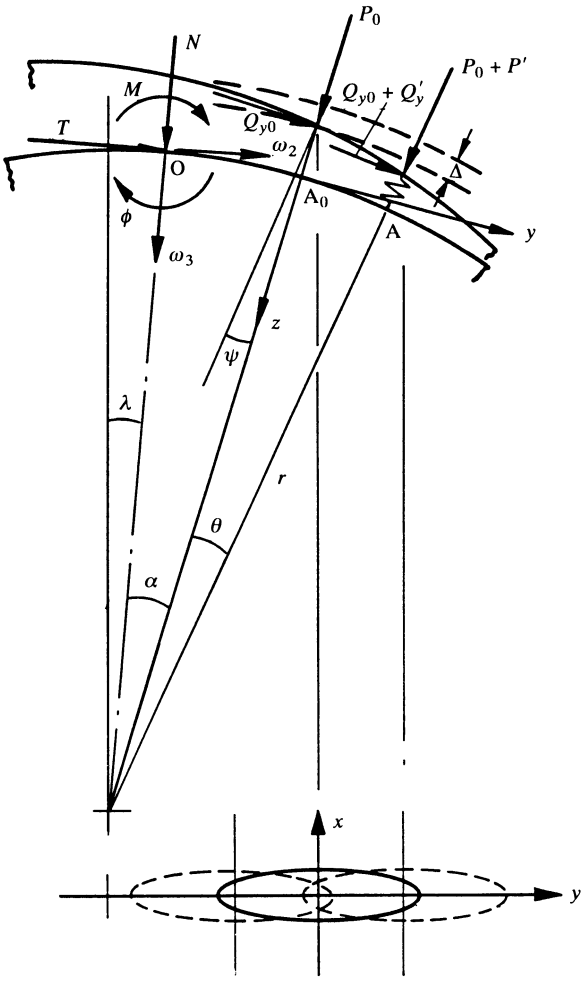

Fig. 7 Geometry of a single moving point of contact between closely conforming surfaces

$$\boldsymbol{c}^t = (1/r)[\cos\alpha \;\; \sin\alpha \;\; -r\cos\alpha] \tag{25}$$

The compression of the Hertz spring at A is given by

$$\delta_z = \Delta - w_3\cos\alpha + (w_2 - r\phi)\sin\alpha \tag{26}$$

If the rolling radius at A_0 is R_1 and that at A is $(R_1 + R'_1)$

$$R'_1 = \rho\sin(\lambda+\alpha)\theta$$

which introduces a fluctuating longitudinal velocity

$$v''_x = -\left(\frac{\rho V}{R_1}\right)\sin(\lambda+\alpha)\theta \tag{27}$$

The motion of the contact point is related to the displacements of the wheel and rail by

$$\begin{bmatrix} v_x' \\ v_y' \\ v_z' \end{bmatrix} + \begin{bmatrix} -v_x'' \\ 0 \\ \mathrm{i}\omega\Delta \end{bmatrix} = \mathrm{i}\omega \begin{bmatrix} 0 & 0 & 0 \\ \cos\alpha & \sin\alpha & 0 \\ -\sin\alpha & \cos\alpha & r\sin\alpha \end{bmatrix} \begin{bmatrix} w_2 \\ w_3 \\ \phi \end{bmatrix}$$

so that

$$\frac{1}{V}\begin{bmatrix} v_x' \\ v_y' \\ v_z' \end{bmatrix} = \mathbf{D}\begin{bmatrix} w_2 \\ w_3 \\ \phi \end{bmatrix} + \boldsymbol{j}\theta + \boldsymbol{e}\Delta$$

with

$$\boldsymbol{j} = \begin{bmatrix} -\rho\sin(\lambda+\alpha)/R_1 \\ 0 \\ 0 \end{bmatrix}, \qquad \boldsymbol{e} = \begin{bmatrix} 0 \\ 0 \\ -\mathrm{i}\omega/V \end{bmatrix} \tag{28}$$

The contact forces, $Q_x = Q_{x0} + Q_x'$ etc. acting at A exert tangential and normal forces $(T_0 + T')$ and $(N_0 + N')$ acting at O, together with a moment $(M_0 + M')$, according to

$$\begin{bmatrix} T' \\ N' \\ M' \end{bmatrix} = \begin{bmatrix} 0 & \cos\alpha & -\sin\alpha \\ 0 & \sin\alpha & \cos\alpha \\ 0 & r(1-\cos\alpha) & r\sin\alpha \end{bmatrix} \begin{bmatrix} Q_x' \\ Q_y' \\ P' \end{bmatrix} + \theta \begin{bmatrix} -P_0\cos\alpha - Q_{y0}\sin\alpha \\ -P_0\sin\alpha + Q_{y0}\cos\alpha \\ P_0 r\cos\alpha + Q_{y0} r\sin\alpha \end{bmatrix} \tag{29}$$

i.e.

$$\begin{bmatrix} T' \\ N' \\ M' \end{bmatrix} = \mathbf{F}\begin{bmatrix} Q_x' \\ Q_y' \\ P' \end{bmatrix} + \theta\boldsymbol{g} \tag{30}$$

The dynamic model of the rail may now be coupled to one of the contact mechanics models described in the previous section to obtain a complete model. For the case of the high-spin model, the result is as shown in the block diagram of Fig. 8. Static input comes in the form of the steady reference state: ξ_{x0}, ξ_{y0} and P_0. Dynamic input is provided by sinusoidal irregularities on the wheel or rail surface in the form of a normal displacement $\Delta\,\mathrm{e}^{\mathrm{i}\omega t}$ at A_0 and a rotation $\psi\,\mathrm{e}^{\mathrm{i}\omega t}$ about A_0. The various vectors and matrices $\boldsymbol{S}$, $\boldsymbol{s}$, $\boldsymbol{c}$, $\boldsymbol{D}$, $\boldsymbol{e}$, $\boldsymbol{F}$, $\boldsymbol{g}$ and $\boldsymbol{j}$ have all been defined in the text, while the box labelled K denotes scalar multiplication by the conformity factor and $\mathbf{H}_\mathrm{R}$ is the matrix of receptances from the rail model. A very similar diagram can be constructed for the low-spin model, but it is not reproduced here. It differs simply in that the box labelled $\boldsymbol{s}$ is absent, and the matrix $\mathbf{S}$ from equation (20) must be replaced by the matrix

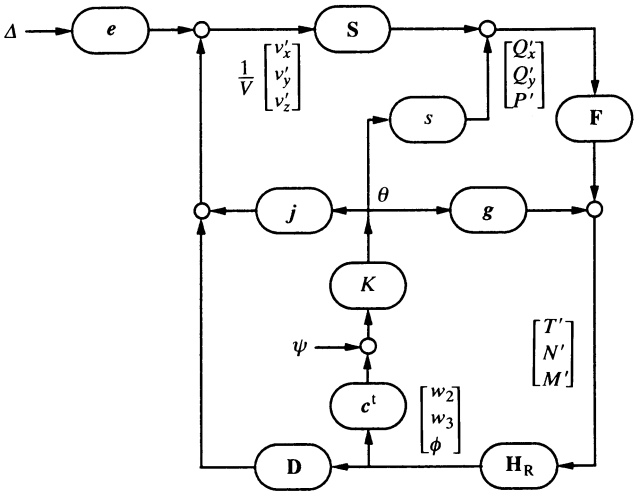

Fig. 8 Block diagram for the complete (linearized) system combining a single moving point of contact (using the high-spin model) with the dynamic response of the rail. Input is provided by the assumed ripple characterized by Δ and ψ, and various output quantities are shown at the appropriate points on the network. Positive signs are assumed at all summing junctions

$$\left[\frac{\mathrm{i}\omega}{V}\mathbf{A} + \mathbf{B}\right]^{-1}$$

from equation (13).

4.2 Two-point contact

If the situation occurs that the radius of curvature of the wheel tread is locally less than that of the rail, two-point contact will take place. This is an extreme case of 'conformal contact', and it is of some interest to analyse in its own right. The detailed form of the wheel and rail profiles determine the positions of the two contact points, A and B, which will not change significantly in response to motion of the rail (see Fig. 9). Since in this case there is no lateral motion of the contact points, $\theta = 0$ in the equations of the previous subsection. A complete model based on two-point contact can be assembled on similar lines to that for moving single-point contact. The input is now naturally expressed as separate vertical 'ripples' of displacement $\Delta_\mathrm{A}\,\mathrm{e}^{\mathrm{i}\omega t}$ at point A and $\Delta_\mathrm{B}\,\mathrm{e}^{\mathrm{i}\omega t}$ at point B. The resultant forces acting on the rail are obtained by adding the contact forces arising at A and B

$$\begin{bmatrix} T' \\ N' \\ M' \end{bmatrix} = \mathbf{F}_\mathrm{A}\begin{bmatrix} Q_x' \\ Q_y' \\ P' \end{bmatrix}_\mathrm{A} + \mathbf{F}_\mathrm{B}\begin{bmatrix} Q_x' \\ Q_y' \\ P' \end{bmatrix}_\mathrm{B} \tag{31}$$

where the matrices $\mathbf{F}_\mathrm{A}$ and $\mathbf{F}_\mathrm{B}$ are given by the expression in equation (29), with $\alpha = \alpha_\mathrm{A}$ and $\alpha = \alpha_\mathrm{B}$ respectively.

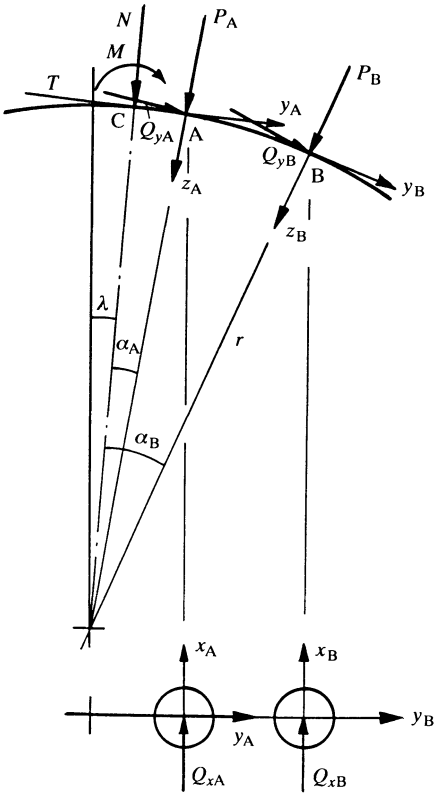

Fig. 9 Geometry of two-point contact, at the points A and B

Since the ellipticity of each contact patch is relatively small, the low-spin contact model is appropriate in this case. The resulting block diagram for the complete two-point contact model is shown in Fig. 10.

5 STABILITY

The next step is to investigate whether the complete closed-loop models described in the previous section exhibit linear instability. If instability were found, it could be hypothesized that small-amplitude oscillators might in fact grow until roll–slip oscillation was occurring. To investigate further would then require a non-linear treatment of the problem, probably via numerical time-marching simulation.

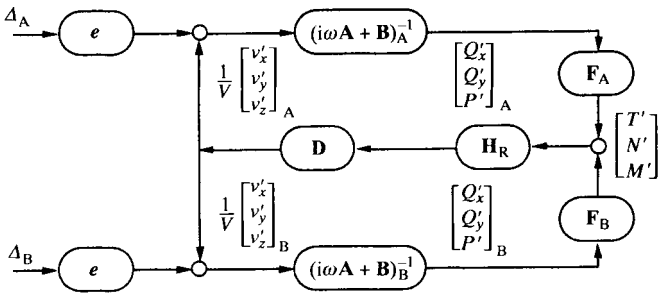

Fig. 10 Block diagram corresponding to Fig. 8, for the complete system assuming two-point contact. Positive signs are assumed at all summing junctions

The somewhat complex interconnected loops of Fig. 8 require rather careful stability analysis. The approach is to decompose the system into smaller units, each having the form of the simple two-block feedback system of Fig. 11. For any such system, standard control theory gives a criterion for stability. The requirement is that for any input signals $w_1(t)$ and $w_2(t)$ with finite energy (in other words, a finite value of the integrated square of the functions over all time), the internal signals $e_1(t)$ and $e_2(t)$ must have finite energy and satisfy the condition of causality. This requirement can be tested using the extended Nyquist theorem (**13**): in terms of the Laplace transfer function matrices $\mathbf{H}_1(s)$ and $\mathbf{H}_2(s)$ the system of Fig. 11 is internally stable if and only if

(a) $\det(\mathbf{I} - \mathbf{H}_1(\infty)\mathbf{H}_2(\infty)) \neq 0$;
(b) the number of right half-plane poles of the product $\mathbf{H}_1(i\omega)\mathbf{H}_2(i\omega)$ is equal to $n_1 + n_2$, where n_1 and n_2 are respectively the number of right half-plane poles (counting multiplicities) of $\mathbf{H}_1$ and $\mathbf{H}_2$; and
(c) $\det(\mathbf{I} - \mathbf{H}_1(s)\mathbf{H}_2(s))$ is non-zero and encircles the origin $n_1 + n_2$ times as s traverses a contour which passes down the imaginary axis from infinity, indenting to the left of any imaginary axis poles, then closes around an arbitrarily large semicircle in the right half-plane.

The particular aim here is to investigate the influence on stability of the conformity factor K. To this end, it is useful to consider first the system with $K = 0$. This leaves the loop shown in Fig. 12a, which has the form of Fig. 11. If this subsystem can be shown to be stable, then it remains to investigate whether the whole system can be destabilized by introducing a non-zero value of K. For this, the

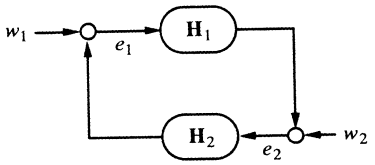

Fig. 11 Block diagram of canonical feedback network

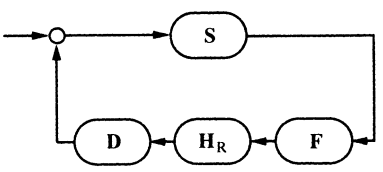

Fig. 12a Block diagram of the system of Fig. 8 when $K = 0$

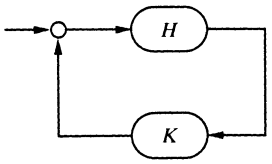

Fig. 12b Block diagram for investigation of the influence of conformity factor on stability

contribution of K can be isolated in the form shown in Fig. 12b, where the box labelled H is simply the whole of the rest of the system apart from the block K. In terms of the matrices defined in the previous section, this transfer function is found by straightforward algebraic manipulation to be given by

$$H = \mathbf{c}^{\mathrm{t}}(\mathbf{I} - \mathbf{H}_{\mathrm{R}}\mathbf{FSD})^{-1}\mathbf{H}_{\mathrm{R}}(\boldsymbol{g} + \mathbf{F}\boldsymbol{s} + \mathbf{FS}\boldsymbol{j}) \tag{32}$$

Again, this system has the form of Fig. 11 so that the Nyquist criterion can be applied directly.

To apply this stability test, the rail model and contact model must be run with particular parameter values. The values selected were those used in a survey of the forced response behaviour of these models to be discussed in the companion paper (**1**), and they are listed in Tables 1 and 2 of that reference. The Nyquist plot for the outer loop representing the case $K = 0$ is shown in Fig. 13a. Figure 13b shows a close-up view of the region near the origin. It is clear that there are no encirclements of the origin, and it follows that the outer loop is internally stable. Two facts must be noted in this connection. First, the rail model is a passive mechanical system and cannot have any poles in the closed right half-plane. Second, the system as it has been formulated has an apparent pole-zero cancellation at zero frequency (pole in **S**, zero in **D**). This arises from the somewhat artificial introduction of the vertical 'creepage' v'_z in place of the vertical displacement δ'_z, and it can be

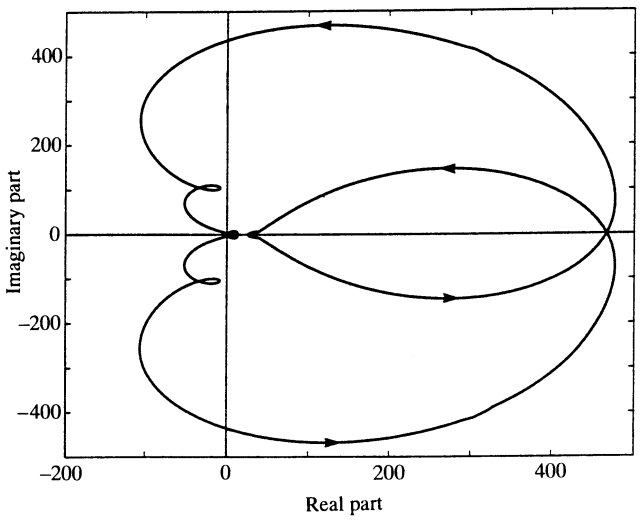

Fig. 13a Nyquist plot for the system of Fig. 12a

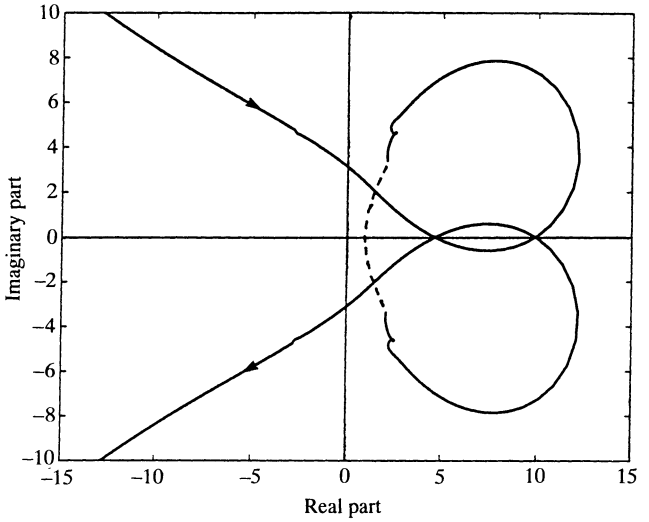

Fig. 13b Expansion of (a) near the origin

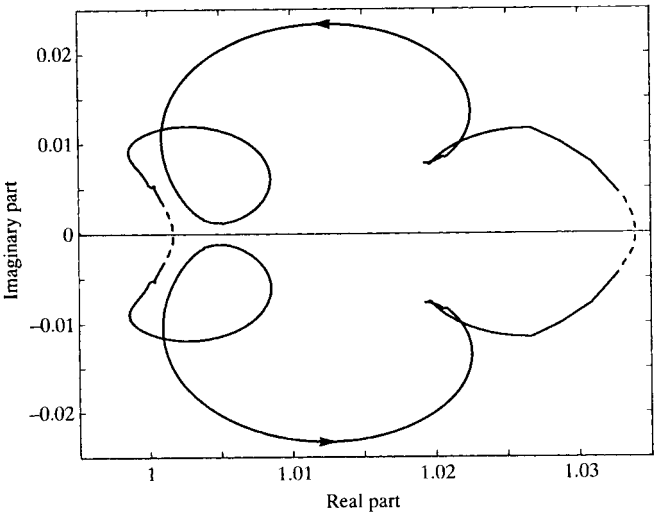

Fig. 13c Nyquist plot for the system of Fig. 12b

readily shown that it does not contribute to the pole count needed for the Nyquist criterion.

A detail to be noted in these Nyquist plots and in the one to follow is that the model has been slightly adjusted at very low frequencies. The assumption of hysteretic damping in the rail pads and ballast produces non-physical results at these low frequencies, manifesting itself in Nyquist loops which do not close. To cure this in a way which is simple but physically sensible, the imaginary parts of the rail receptances at very low frequencies have been forced to tend to zero, producing artificial kinks in the Nyquist plots but giving the correct topology for the purpose of the Nyquist criterion.

The Nyquist plot for the conformity factor loop of Fig. 12b is shown in Fig. 13c, for the particular case having $K = 1$. It shows no encirclements of the origin, and so the introduction of the additional feedback loops via K does not produce instability. Since changing the value of K

simply amounts to a scaling of this plot relative to the point (1,0), this remains true for all possible values of K. This result has been confirmed by checking the Nyquist criterion for the complete system at a range of values of K.

The corresponding stability analysis has also been carried out using the low-spin contact model of Appendix 1. The Nyquist plots corresponding to those of Fig. 13 are different in detail, but are qualitatively very similar to those shown here for the high-spin model. Neither loop encircles the origin.

The conclusion is that the single-point contact model is stable, for all values of the conformity factor K, at least when coupled to the continuously supported rail model employed here, with parameter values appropriate to British Rail track. The dominant physical reason for this strong stability appears to be associated with the high level of vibration damping provided by the infinite rail model—energy in oscillation at the contact region is simply lost by radiation of bending and torsional waves along the rail. This conclusion is in a sense disappointing, since it shows that the model analysed here does not immediately lead to an explanation of some of the findings on the Vancouver Skytrain system (scratch marks, and a variation of corrugation wavelength with train speed suggesting roll–slip oscillation). It remains possible that instability might arise if further features of the physical system were included in the model. Candidates might be wheel resonances, and perhaps the constraining effect of adjacent wheels of the vehicle, reflecting back some of the vibrational energy radiated along the rail. These are matters for future research.

6 CONCLUSIONS

A dynamic model of the wheel–rail system has been set up on the basis of a rigid wheel and a continuously supported rail. Receptance curves for excitation at the railhead by vertical force, horizontal force or moment have been calculated over the range 0–2 kHz. These show good agreement with the model described by Ripke (**9**), except in certain narrow frequency bands which are strongly influenced by the presence of discrete supports.

Two contact mechanics models, which relate dynamic creep forces to fluctuating creepages, have been proposed. The first applies under conditions of low-spin creepage, and includes the transient effect which leads to frequency dependent creep coefficients. The second applies under the conditions of high spin which arise with close conformity, when the contact region becomes highly elliptical. Tangential elastic deformations, and hence transient effects, are neglected in this model, but they are in any case expected to be small under conditions of close conformity and high spin.

The effect of close conformity has been modelled in two separate ways. In the first, the wheel and rail are assumed to touch at one point, giving rise to a highly elliptical contact region and high spin. Dynamic torsion of the rail causes the point of contact to move laterally across the railhead. In the second model of conformity, two separate points of contact are assumed. These are taken to be circular and not to move laterally across the railhead. In this case, spin is effectively taken into account by imposing a difference in the steady longitudinal creepages at the two points of contact.

The stability of motion under these models has been investigated, using linear theory, and it has been found that the system is stable within the expected range of parameters and conformity. This conclusion holds for both low-spin and high-spin contact models. It remains to investigate the forced response of the models to a pre-existing surface ripple on the rail or wheel, to determine whether wear processes might be expected to deepen or to erase the ripple, and hence to lead to growth or decay of short-pitch corrugations. This issue is discussed in Part 2 of this paper (**1**).

ACKNOWLEDGEMENTS

The authors thank B. Ripke and S. Müller for help with, and permission to reproduce, the comparisons with the Berlin rail model (**9**). The work reported here was carried out with the support of a grant from ERRI committee D185.

REFERENCES

1 **Bhaskar, A., Johnson, K. L.** and **Woodhouse, J.** Wheel–rail dynamics with closely conformal contact. Part 2: forced response, results and conclusions. *Proc. Instn Mech. Engrs, Part F*, 1997, **211** (F1), 27–40.

2 **Grassie, S. L.** and **Kalousek, J.** Rail corrugation: characteristics, causes and treatments. *Proc. Instn Mech. Engrs*, 1993, **207** (F2), 57–68.

3 **Hempelmann, K.** and **Knothe, K.** An extended linear model for the prediction of short wavelength corrugation. *Wear*, 1996, **191**, 161–169.

4 **Frederick, C. O.** A rail corrugation theory. Proceedings of the 2nd International Conference on *Contact Mechanics of Rail/Wheel Systems*, University of Rhode Island, 1986, pp. 181–211 (University of Waterloo Press).

5 **Valdivia, A.** The interaction between high-frequency wheel–rail dynamics and irregular rail wear. *VDI-Fortschrittsbericht*, Reihe 12, Nr.93, 1988, Dusseldorf.

6 **Kalousek, J.** and **Johnson, K. L.** An investigation of short pitch wheel and rail corrugation on the Vancouver mass transit system. *Proc. Instn Mech. Engrs, Part F*, 1992, **206** (F2), 127–135.

7 **Grassie, S. L., Gregory, R. W.** and **Johnson, K. L.** The behaviour of railway wheelsets and track at high frequencies of excitation. *J. Mech. Engng Sci.*, 1982, **24**, 103–111.

8 **Thompson, D. J.** Wheel–rail noise generation, Part III: rail vibration. *J. Sound Vibration*, 1993, **161**, 421–446.

9 **Ripke, B.** and **Knothe, K.** Die unendlich lange Schiene auf

diskreten Schwellen bei harmonischer Einzellastanregung, *VDI Fortschritte*, Reihe 11, N.155, 1991, Dusseldorf.
10 **Johnson, K. L.** *Contact Mechanics*, 1985 (Cambridge University Press).
11 **Kalker, J. J.** *Three-dimensional Elastic Bodies in Rolling Contact*, 1990 (Kluwer, Dordrecht).
12 **Gross-Thebing, A.** Lineare Modellierung des instationaren Rollcontakts von Rad und Schiene, *VDI-Fortschritte*, Reihe 12 Nr.199, 1993, Dusseldorf.
13 **Desoer, C. A.** and **Vidyasagar, M.** *Feedback Systems: Input–Output Properties*, 1975 (Academic Press, New York).
14 **Frederick, C. O.** A rail corrugation theory which allows for contact patch size. Proceedings of Symposium on *Rail Corrugation Problems*, Berlin, 1991 (ILR-Bericht 59).
15 **Johnson, K. L.** The effect of a tangential contact force on the rolling motion of an elastic sphere on a plane. *Trans. ASME, J. Appl. Mechanics*, 1958, **25**, 339–346.
16 **Mindlin, R. D.** Compliance of elastic bodies in contact. *Trans. ASME, J. Appl. Mechanics*, 1949, **16**, 259–268.
17 **Mindlin, R. D.** and **Deresiewicz, H.** Elastic spheres in contact under varying oblique forces. *Trans. ASME, J. Appl. Mechanics*, 1953, **20**, 327–345.

APPENDIX 1

Low-spin contact model

The steady creep equations (5a and b) may be written

$$\xi_x = k_1 P^{1/3}\left(\frac{Q_x}{Q}\right)\left[1-\left(1-\frac{Q}{\mu P}\right)^{1/3}\right] = k_1 f_x \tag{33a}$$

$$\xi_y + k_2 P^{1/3} = k_1 P^{1/3}\left(\frac{Q_y}{Q}\right)\left[1-\left(1-\frac{Q}{\mu P}\right)^{1/3}\right] = k_1 f_y \tag{33b}$$

where

$$k_1 = \frac{3\mu}{C_{00}}\left[\frac{16}{9(1-\nu)^2 R_e^2 G}\right]^{1/3} \tag{34}$$

and

$$k_2 = \frac{C_{23}}{C_{00}}\frac{\sin(\lambda+\alpha)}{R_1}\left[\frac{3(1-\nu)R_e}{4G}\right]^{1/3} \tag{35}$$

Kalker's creep coefficients as a function of (a/b) may be expressed approximately by

$$C_{00} = 1/2(C_{11}+C_{22}) = -\left[2.84 + 1.20\left(\frac{a}{b}\right)\right] \tag{36}$$

and

$$C_{23} = 0.40 + 1.05\left(\frac{a}{b}\right) \tag{37}$$

The effect of small changes in Q_x, Q_y and P from a reference state Q_{x0}, Q_{y0} and P_0 is found by differentiation of (33a and b)

$$\frac{\partial f_x}{\partial Q_x} = \frac{P^{1/3}Q_y^2}{Q^3}\left[1-\left(1-\frac{Q}{\mu P}\right)^{1/3}\right] + \frac{1}{3\mu P^{2/3}}\left(\frac{Q_x}{Q}\right)^2\left(1-\frac{Q}{\mu P}\right)^{-2/3} \tag{38a}$$

$$\frac{\partial f_y}{\partial Q_y} = \frac{P^{1/3}Q_x^2}{Q^3}\left[1-\left(1-\frac{Q}{\mu P}\right)^{1/3}\right] + \frac{1}{3\mu P^{2/3}}\left(\frac{Q_y}{Q}\right)^2\left(1-\frac{Q}{\mu P}\right)^{-2/3} \tag{38b}$$

$$\frac{\partial f_x}{\partial Q_y} = \frac{\partial f_y}{\partial Q_x} = \frac{1}{3\mu P^{2/3}}\frac{Q_x Q_y}{Q^2}\left(1-\frac{Q}{\mu P}\right)^{1/3} - \frac{P^{1/3}Q_x Q_y}{Q^3}\left[1-\left(1-\frac{Q}{\mu P}\right)^{1/3}\right] \tag{38c}$$

$$\frac{\partial f_x}{\partial P} = \frac{1}{3P^{2/3}}\frac{Q_x}{Q}\left[1-\left(1-\frac{Q}{\mu P}\right)^{-2/3}\right] \tag{38d}$$

$$\frac{\partial f_y}{\partial P} = \frac{1}{3P^{2/3}}\frac{Q_y}{Q}\left[1-\left(1-\frac{Q}{\mu P}\right)^{-2/3}\right] \tag{38e}$$

The matrix **B** is now defined by

$$\mathbf{B} = k_1\begin{bmatrix} \dfrac{\partial f_x}{\partial Q_x} & \dfrac{\partial f_x}{\partial Q_y} & \dfrac{\partial f_x}{\partial P} \\ \dfrac{\partial f_y}{\partial Q_x} & \dfrac{\partial f_y}{\partial Q_y} & \left(\dfrac{\partial f_y}{\partial P} - \dfrac{k_2}{k_1}P^{-2/3}\right) \\ 0 & 0 & 0 \end{bmatrix} \tag{39}$$

An elastic rolling contact with creepage has a contact area which is divided into a region of adhesion ('stick') and one of slip. A complete solution to the problem of transient creep requires tangential elastic displacements of the two bodies at the interface to satisfy the appropriate conditions of stick and slip throughout the contact area ((**10**), §8.1). This was first achieved by Kalker (**11**) in line contact with longitudinal creepage only. A numerical approach to a complete solution with general creepage has been obtained by Gross-Thebing (**12**). A simplified approach, using the elastic foundation or 'wire–brush' contact model, has been employed by Frederick (**14**) in his corrugation theory. The closed-form expressions for non-linear steady creepage (33a and b) are based on the assumption that the stick area is an ellipse, similar to the contact ellipse, and tangential to it at the leading point $(-a, 0)$. This early theory (**15**) was found to have errors of up to 25 per cent in the linear creep coefficients compared with Kalker's exact values (**11**).

However, a good fit with experiment is obtained if the linear coefficients are replaced by Kalker's values, while retaining the functional form of f_x and f_y.

The compliance of a stationary contact with an elliptical stick area has been found by Mindlin (**16**), with the results

$$\delta_x = \frac{C_{44}}{2Gc}\frac{3\mu P}{2}\frac{Q_x}{Q}\left[1-\left(1-\frac{Q}{\mu P}\right)^{2/3}\right] \tag{40a}$$

$$\delta_y = \frac{C_{55}}{2Gc}\frac{3\mu P}{2}\frac{Q_y}{Q}\left[1-\left(1-\frac{Q}{\mu P}\right)^{2/3}\right] \tag{40b}$$

where for Poisson's ratio $\nu = 0.3$

$$C_{44} = -0.85\sqrt{(a/b)}[1 + 1.14\log_{10}(b/a)] \tag{41a}$$

$$C_{55} = -0.85\sqrt{(a/b)}[1 + 1.57\log_{10}(b/a)] \tag{41b}$$

The effect of small changes in Q'_x, Q'_y, P' from the reference state Q_{x0}, Q_{y0}, P_0 depends upon whether the forces are increasing or decreasing [see Mindlin and Deresiewicz (**17**)]. The relationship of equation (40) is plotted in Fig. 14 for $Q_{y0} = 0$; $P = P_0$ and $P = P_0 + P'$ where P' is negative. The reference state is indicated by point A. A small increase in tangential force Q'_x causes a move to point B such that

$$\delta'_x = \left(\frac{\partial\delta_x}{\partial Q_x}\right)_{\mathrm{A}} Q'_x \tag{42}$$

where $(\partial\delta_x/\partial Q_x)_{\mathrm{A}}$ is the derivative of equation (40a). On the other hand a reduction in Q_x from either A or B causes a move to point C, D or E, such that

$$\delta'_x = \left(\frac{\partial\delta_x}{\partial Q_x}\right)_0 Q'_x \tag{43}$$

where $(\partial\delta_x/\partial Q_x)_0$ is the derivative at the origin. Reloading

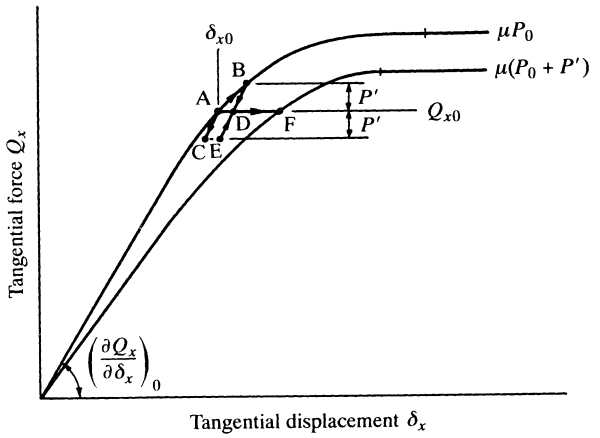

Fig. 14 Incremental changes in tangential force due to small changes in tangential displacement δ_x and normal force P_0 [from reference (**16**)]

from C, D or E results in changes given by equation (43). Hence the compliance of an oscillation in Q''_x about Q_{x0} is also given by equation (43). A small increase P', keeping Q_x and Q_y constant, causes the contact area to grow without any change of tangential traction, so that $\delta'_x = \delta'_y = 0$. A reduction in P_0 by P' causes a move from state A to F in which

$$\delta'_x = \left(\frac{\partial\delta_x}{\partial P}\right)_{\mathrm{A}} P' \tag{44}$$

A subsequent increase in P from F causes no further changes in δ_x; nor does an oscillatory variation in P. Extending the reasoning to a reference state in which both Q_{x0} and Q_{y0} are non-zero, during an increase in Q (i.e. $Q' > 0$) together with a decrease in P (i.e. $P' < 0$), the changes in displacement from a reference state A are given by

$$\begin{bmatrix}\delta'_x\\ \delta'_y\\ \delta'_z\end{bmatrix} = \begin{bmatrix}\left(\frac{\partial\delta_x}{\partial Q_x}\right)_{\mathrm{A}} & \left(\frac{\partial\delta_x}{\partial Q_y}\right)_{\mathrm{A}} & \left(\frac{\partial\delta_x}{\partial P}\right)_{\mathrm{A}}\\ \left(\frac{\partial\delta_y}{\partial Q_x}\right)_{\mathrm{A}} & \left(\frac{\partial\delta_y}{\partial Q_y}\right)_{\mathrm{A}} & \left(\frac{\partial\delta_y}{\partial P}\right)_{\mathrm{A}}\\ 0 & 0 & \left(\frac{\partial\delta_z}{\partial P}\right)_{\mathrm{A}}\end{bmatrix}\begin{bmatrix}Q'_x\\ Q'_y\\ P'\end{bmatrix} \tag{45}$$

For oscillating variations $Q'_x e^{i\omega t}$ etc. equation (45) becomes

$$\begin{bmatrix}\delta'_x\\ \delta'_y\\ \delta'_z\end{bmatrix} = \begin{bmatrix}\left(\frac{\partial\delta_x}{\partial Q_x}\right)_0 & 0 & 0\\ 0 & \left(\frac{\partial\delta_y}{\partial Q_y}\right)_0 & 0\\ 0 & 0 & \left(\frac{\partial\delta_z}{\partial P}\right)_{\mathrm{A}}\end{bmatrix}\begin{bmatrix}Q'_x\\ Q'_y\\ P'\end{bmatrix} \tag{46}$$

where

$$a_{11} \equiv \left(\frac{\partial\delta_x}{\partial Q_x}\right)_0 = \frac{C_{44}}{2Gc}$$

$$a_{22} \equiv \left(\frac{\partial\delta_y}{\partial Q_y}\right)_0 = \frac{C_{55}}{2Gc}$$

and

$$a_{33} \equiv -\left(\frac{\partial\delta_z}{\partial P}\right)_{\mathrm{A}}$$

is the compliance of the Hertz spring given by equation (11) in the text. The matrix in equation (46) is denoted by **A**.

Under conditions of varying creepage from a reference state, it is now assumed that the instantaneous relative velocity vector $\boldsymbol{v}'$ between the two surfaces can be expressed by the simple summation of the *steady* creepage and the rate of change of the *static* compliance, i.e.

$$\boldsymbol{v}' = V\boldsymbol{\xi}' + \frac{\mathrm{d}\boldsymbol{\delta}}{\mathrm{d}t} \tag{47}$$

where V is the vehicle speed. In terms of $\boldsymbol{Q} = [Q_x,\ Q_y,\ P]^{\mathrm{t}}$, equation (47) becomes

$$\boldsymbol{v}' = V\mathbf{B}\boldsymbol{Q}' + \mathbf{A}\frac{\mathrm{d}\boldsymbol{Q}}{\mathrm{d}t} \tag{48}$$

For harmonic variations in $\boldsymbol{Q}'$ of angular frequency ω

$$(1/V)\boldsymbol{v}' = [\mathbf{B} + (\mathrm{i}\omega/V)\mathbf{A}]\boldsymbol{Q}' \tag{49}$$

APPENDIX 2

High-spin contact model

In order to incorporate lateral creepage ξ_y, and its interaction with longitudinal and spin creepage in a simple way, choose a representative strip at a distance L from the spin pole, where $y = L$ locates the line of action of Q_{x1} when $s = 0$, i.e. when $\xi_x = 0$. Thus

$$L = M_{z1}(0)/Q_{x1}(0) = (3/16)\mu Pb/(1/2)\mu P = (3/8)b \tag{50}$$

Now assume that L remains unchanged for all values of s, so that

$$\xi''_{x1} = -\frac{\omega_z b}{V}\frac{3}{8}(1-s) = -\xi_s(1-s) \tag{51a}$$

and

$$\xi''_{x2} = +\frac{\omega_z b}{V}\frac{3}{8}(1+s) = +\xi_s(1+s) \tag{51b}$$

where

$$\xi_s = \frac{3}{8}\frac{\omega_z b}{V}$$

is the representative creepage due to spin. Now take

$$\frac{Q_{y1}}{Q_{x1}} = \frac{\xi_y}{\xi''_{x1}} \qquad \text{and} \qquad \frac{Q_{y2}}{Q_{x2}} = \frac{\xi_y}{\xi''_{x2}}$$

Writing

$$\xi_1 = (\xi''^2_{x1} + \xi_y^2)^{1/2} \tag{52a}$$

and

$$\xi_2 = (\xi''^2_{x2} + \xi_y^2)^{1/2} \tag{52b}$$

$$r_1 \equiv \frac{\xi_1}{\xi_s} = [(1-s)^2 + t^2]^{1/2}$$

and

$$r_2 \equiv \frac{\xi_2}{\xi_s} = [(1+s)^2 + t^2]^{1/2}$$

where $t = \xi_y/\xi_s$.

Making use of equation (17a and b) from the text, for which $\xi_y = 0$, the following are obtained

$$Q_{x1} = \frac{\mu P}{4}\frac{(1-s)}{r_1}(2 - 3s + s^3) \tag{53a}$$

and

$$Q_{x2} = -\frac{\mu P}{4}\frac{(1+s)}{r_1}(2 + 3s - s^3) \tag{53b}$$

$$Q_{y1} = -\frac{\mu P}{4}\frac{t}{r_1}(2 - 3s + s^3) \tag{54a}$$

and

$$Q_{y2} = -\frac{\mu P}{4}\frac{t}{r_2}(2 + 3s - s^3) \tag{54b}$$

$$M_{z1} = -\frac{3\mu P}{16}\frac{(1-s)}{r_1}(2 - 3s + s^3) \tag{55a}$$

and

$$M_{z2} = -\frac{3\mu P}{16}\frac{(1+s)}{r_2}(2 + 3s - s^3) \tag{55b}$$